Materials Science & Engineering A 801 (2021) 140368

Contents lists available at ScienceDirect

Materials Science & Engineering A

journal homepage: http://www.elsevier.com/locate/msea

Study of residual stress and microstructural evolution in as-deposited and inter-pass rolled wire plus arc additively manufactured Inconel 718 alloy after ageing treatment

Jan Hönnige [a], Cui Er Seow [b,c], Supriyo Ganguly [a,*], Xiangfang Xu [a], Sandra Cabeza [d], Harry Coules [c], Stewart Williams [a]

[a] Welding Engineering and Laser Processing Centre, Cranfield University, MK43 0AL, Cranfield, UK
[b] National Structural Integrity Research Centre, TWI Ltd, Granta Park, Great Abington, Cambridge, CB21 6AL, UK
[c] Department of Mechanical Engineering, University of Bristol, Bristol, BS8 1TR, UK
[d] Institut Laue-Langevin, 71 Avenue des Martyrs, 38000, Grenoble, France

ARTICLE INFO

Keywords:
Additive manufacture
Neutron diffraction
Nickel
Residual stress
Microstructure

ABSTRACT

The manufacture of structural components made from nickel-based super alloys would benefit from the commercial advantages of Wire + Arc Additive Manufacturing (WAAM), as it is commonly expensive to process using other conventional techniques. The two major challenges of WAAM are process residual stress and undesired microstructure. Residual stress causes part distortion and build failures, while the as-deposited microstructure does not allow the common heat-treatment to be effective in achieving the desired mechanical properties. This paper focuses on understanding the microstructural features, phase formation and three-dimensional residual stress state variation in as-deposited and inter-pass rolled conditions and after solutionising, quenching and ageing. The thermal history from successive deposition and cold working were correlated to the phase formation and macro residual stress formation and subsequent evolution. The {311} family of crystallographic planes were used as atomic strain gauge to determine the macrostrain and analysis of three dimensional stress state in different processing conditions. The measured strain were corrected for the compositional variation by measuring EDM machined d_0 specimens manufactured under similar processing conditions. While the as-deposited part show significant stress redistribution and distortion after removal from the main fixture, inter-pass rolling was found to reduce part distortion significantly, the residual stress profile after inter-pass rolling showed highest tensile magnitude near the substrate while near the top of the deposit it was compressive as can be expected from the rolling process. The other two beneficial effects of inter-pass rolling on the microstructure are mitigation of the formation of undesired Laves-phase, thereby improving the response to solution treatment and aging together with significantly reduced grain size and texture. The application of inter-pass rolling reduces the potential part complexity, which however does not prevent the manufacture of common candidate parts, which are typically 1-to-1 replacements of forged, cast or machined from solid.

1. Introduction

Wire + Arc Additive Manufacturing (WAAM) is a directed-energy-deposition (DED) process that is used for the manufacture of medium-complexity near-net-shape components [1]. Even though it is a metal additive process, typical applications target the 1-to-1 replacement of preform components that are otherwise produced by casting, forging or machining from solid. Compared to those, the advantages of WAAM are reductions of cost, material waste and lead time. Common materials for WAAM are structural alloys, such as steels and aluminium alloys. The metals that exploit the advantages of WAAM the most, are typically high-value, expensive to process and tough-to-machine alloys, such as titanium [2] and Inconel (IN) [3]. The WAAM deposition of the latter was first reported by Clark et al. [4,5] reporting better part quality using tungsten-inert-gas (TIG) as opposed to metal-inert-gas (MIG) power sources. Recent work [6] has also demonstrated that coaxial deposition is possible.

Nickel-based alloys are amongst the most complex alloy systems and

* Corresponding author.
E-mail address: s.ganguly@cranfield.ac.uk (S. Ganguly).

https://doi.org/10.1016/j.msea.2020.140368
Received 27 April 2020; Received in revised form 17 August 2020; Accepted 6 October 2020
Available online 14 October 2020

have a good corrosion resistance and mechanical properties. Creep resistance of the solid solution strengthened IN718 is due to the slow diffusion speed of Niobium and other large atoms [7], preserving the excellent properties at high temperatures [8–10]. It requires certain manufacturing routes to achieve the characteristic microstructure and outstanding mechanical properties, including thermal and mechanical processing [11,12]. The main strengthening phase in IN718 is γ'' (Ni_3Nb), which exist as small coherent platelets that occur after aging a solution treated microstructure. Some strengthening is also contributed by γ' (Ni_3 [Al,Ti]) [13], but due to low Ti and Al in the alloy composition this phase occupies a smaller volume fraction [14]. The crystal structure of the parent γ and strengthening γ′ phase is face-centred-cubic (fcc), but that of the γ'' phase is body-centred tetragonal (bct), inducing strong coherency strains [13]. These strengthening phases are typically precipitated during aging treatments [15,16]. It is, however, possible that the hardening constituents form other undesired phases, when they occur during slow cooling during solidification or processing at too high-temperatures. In IN718 these are the δ phase [17], an orthorhombic form of Ni_3Nb and the hexagonal niobium and molybdenum-rich Laves phase [18] ($(Ni,Fe,Cr)_2(Nb,Mo,Ti)$) and both are undesired and a challenging problem in DED of IN718 [19,20].

Residual stresses are one of the major challenges in WAAM. They can cause serious part distortion or failure during manufacture or in service. The development of residual stresses in WAAM and the consequent distortion using other structural metals, like steel [21,22], titanium [23–25] and aluminium [26], have been explored recently. Single-pass WAAM deposits typically develop constant tensile residual stresses along the height of the deposit that can reach near-yield strength during the build of steel and aluminium walls [21,26], and 60% of yield strength in titanium deposits [24]. After unclamping the part distorts, which redistributes the stresses to equilibrium. The redistributed stress is a superposition of the initial stress and bending distortion stress and typically shows a linear drop towards the top, while the stress below and above the neutral axis increases and decreases respectively [21–27], which is explained in detail elsewhere [27]. Also the effect of residual stress on static [28] and dynamic properties, such as fatigue life [REF – Presentation ECRS], fracture toughness and crack growth [29,30] were investigated. Influences of stress on the formation of the important γ'' precipitates in IN718 was reported as well [13].

Some work has been done on residual stresses in additively manufactured Inconel using different processes or alloys [31–35]. The deposited layer develops large tensile residual stresses, but the thermo-mechanical interaction with the surrounding material also relieves the stresses of the previous layers, depending on the magnitude of the stress and the transient thermal history [34]. SLM-deposited IN718 can develop stresses larger than 1000 MPa, reaching the materials yield strength. These stresses however were measured at the surface, while the bulk residual stresses in the same specimen were not higher than 300 MPa [33], which was attributed to annealing by thermal processing of the subsequent layers. Smetannikov et al. [36] deposited an IN718 wall of 10 layers with the WAAM process using a TIG power source. They used thermocouple recordings and the final distortion to validate their transient simulation. Maximum residual stresses after unclamping did not exceed 380 MPa. It is not clear whether relaxation of previous layers was accounted for, but slightly larger tensile stress in the top-most layer compared to the previous layer can be identified. This would mean that the magnitude of peak tensile residual stress in WAAM is much lower in magnitude compared to SLM.

Conventional manufacturing routes can also induce residual stresses that need to be mitigated [11], meaning that WAAM does not introduce an entirely new challenge. Since IN718 was developed for high strength and good fatigue resistance at high temperatures, it is an excellent material candidate for the 1-to-1 replacement of forging by WAAM. It can be deposited using coaxial heat sources [6] or with cold wire feed [37,38]. Another remaining challenge in DED of nickel-based alloys is a strong crystallographic texture [39,40], which causes anisotropic stiffness [41], reduced strength [37] and furthermore complicates diffraction techniques.

Process residual stresses can be expected to be eliminated during solution treatment of the obligatory heat treatment of IN718. Substantial residual stresses however can subsequently arise during the quench, reaching more than 350 MPa in both tension and compression [42], which is probably not further affected during the aging treatment [43,44].

Neutron diffraction can be used to determine multiaxial stresses in bulk metal. Good knowledge of the material and careful procedure and post-processing is required for obtaining sound results [45]. Several factors should be accounted for such as: large grain size, texture, appropriate stress-free reference specimen, elastic constants, second phases and overlapping diffraction peaks. All of these potential sources of error can occur in additively manufactured nickel-base alloys [10,20,32,37,41]. The experimental determination of residual stresses in a component is therefore complicated, time-consuming and represents the final stress state only [22–26], rather than the evolution of the same. Transient numerical simulations are needed to understand the stress development during the additive WAAM deposition [21]. For IN718 this requires precise understanding of transient material behaviour at any temperature [46], which have to be determined experimentally for additively processed alloy [7]. Simulations are therefore required to account for the residual stress development during the DED process, to design appropriate fixtures for instance, but they need to be validated by stress measurements on representative components.

Since WAAM is descended from welding, similar techniques to control residual stresses can be adopted [47]. Thermal techniques include optimising the deposition strategy, pre-heating or active cooling, which all mitigate the thermal strain as it develops [48–50]. The strategies are not trivial or universally applicable for all materials and processes. Inconel and titanium for instance can behave contrarily to certain thermal strategies [51]. An effective mechanical technique is cold rolling [52–54]. With WAAM this technique is called inter-pass rolling and applied after each deposited layer. It is effective for the mitigation of residual stress and to eliminate distortion in aluminium structures [26,55], but the effectiveness on steel and titanium structures is limited [22,23]. In order to assure a complete stress-free component with more complex features, such as intersection, thermal stress relief remains the only reliable and practical solution [25].

During the research on stress control, a different beneficial effect on WAAM was observed. Inter-pass rolling can be used to eliminate texture and reduce grain size in Ti–6Al–4V [56] or to eliminate porosity in aluminium deposits [55], which both improve the mechanical properties significantly [57,58]. A special technique to eliminate porosity in additive manufacturing is hot-isostatic-pressing (HIPing). Unfortunately the closed pores during HIPing can return at elevated temperatures [59]. This makes post-process HIPing redundant with IN718, which is intended to be used for high-temperature applications. Those pores that were eliminated by inter-pass rolling on the other hand do not reoccur during heat treatment of aluminium-copper alloy [55]. Special thermo-mechanical processing routes including hot rolling can lead to properties that exceed AMS specification by far [60]. The advantageous effect of inter-pass rolling on the microstructure and mechanical properties was also discovered for WAAM-built IN718 components [37].

The aim of this paper is to investigate the residual stress during the WAAM deposition of IN718 alloy, which needs to be known to determine substrate dimensions and design adequate fixtures that prevent part distortion or failure during the deposition and can also be used to validate process models. It will furthermore examine whether cold rolling can mitigate these residual stresses, alongside with the improvement in the material's microstructure and mechanical properties. Finally the residual stresses will be assessed in both structures, with and without inter-pass rolling, after solution heat-treatment, quenching and ageing (SQA), which represents the material's condition in application. This paper will therefore complement the experimental research

on the stress development during the WAAM deposition of structural metals [22–26].

2. Methodology

2.1. Production of specimen

A 1.2 mm diameter IN718 wire was used to deposit the walls on a 200 × 64 × 6 mm^3 IN718 substrate (HAYNES® 718 alloy) with the compositions shown in Table 1. An ABB robotic arm was synchronised with a Fronius VR 7000 power source and manipulated the cold metal transfer (CMT) torch during the deposition [6]. The clamping and the cross-sectional dimensions of the deposit are for comparison the same as during previous investigations using titanium and aluminium alloy [24,26]. The travel speed (TS) to deposit the 180 mm long layers was 6 mm/s at 7 m/min wire feed speed (WFS), yielding a TS to WFS ratio of 19.4 and a deposition rate of 3.87 kg/h. To accommodate for the heat sink effect on the first layer [6], the wire feed speed was increased by 25% to increase the heat input. Four specimens were produced using identical parameters and conditions, of which two were inter-pass rolled (IR) with 50 kN rolling load using the machine described elsewhere [55,56]. The as-deposited (AD) reference specimen remained clamped on the portable jig for the time being to measure and compare the residual stresses before and after unclamping. The other AD specimen and one of the IR specimen were solution heat treated, quenched and aged (SQA). A height gauge and Vernier calipers were used to measure the height and width of each layer, as well as the distortion of each specimen [26]. The specimens were completed once they were 21 mm height, which took 9 layers for the AD and 11 layers for the IR specimens. The SQA treatment on IN718 was performed according to AMS-5662 M. Solution treatment for 1 h (970 °C–980 °C) and water quenching was followed by aging at 718 °C for 8 h, furnace cooling to 620 °C for 2 h and holding that temperature for another 8 h. The four specimens are therefore: AD (still clamped to the portable jig), IR, AD + SQA and IR + SQA.

2.2. Neutron diffraction stress analysis

Non-destructive bulk residual stress determination was carried out on the SALSA neutron diffractometer at the Institut Laue-Langevin, France [45]. Angle-dispersive neutron diffraction was used to determine the strain and analyse the stress in the additive built walls as previously described in Ref. [22]. A monochromated neutron beam of wavelength 1.62 Å was selected resulting in a detector positioning at 2θ = 96.2° for the Ni-{311} plane of the FCC unit cell, commonly used for stress analysis, since it is relatively insensitive to inter-granular strain and its' stiffness is closest to the macroscopic one in conventional [61] and additively manufactured [7,62] nickel-based alloys. A gauge volume of 2 × 2 × 2 mm^3 was defined by oscillating radial collimators on the incoming and diffracted beams. The setup on the beamline is shown in Fig. 1 (a) and the beam path with the locations of the gauge volumes in the specimen is drawn in the schematic in Fig. 1 (b). In this configuration the longitudinal strain is scanned with a step distance of 2 mm along the built direction. The sample was rotated twice by 90° in order to align the scattering vector Q (fixed) with the other two principal strain directions. The mapping of points considered are in building direction, longitudinal and transverse to the wall. It should be noted that the gauge volumes to record the principal strain components overlapped slightly. The use of the cradle allowed the use of a single setup to program and scan all three principal directions. Oscillation of the hexapod of ±4° around the vertical axis was deployed to improve the statistics of the diffraction pattern of the mm-sized coarse-grained material [37].

Reference walls were build using all 4 processing conditions to determine the macro stress free lattice spacing d_0, along the built direction which would allow positional correction of the measured strain which is sensitive on the processing route [26,63]. Wire batch, deposition parameters, dwell time and all other processing conditions were kept the same to produce the most representative stress free reference allowing the compositional variation which would influence the lattice spacing for the measured family, {311}, of crystallographic planes. An electro discharge machining of comb specimens to relieve the macroscopic stress [64] were performed which would ensure minimal impact on the lattice structure of the specimens due to the machining process. The comb consisted of 2.9 × 2.9 × 10 mm teeth, each 3 mm apart in z direction, which were measured 1.5 mm away from the tip in all three orientations. The d_0 for the stress measurement points that did not coincide with d_0 locations due to the comb spacing was interpolated for the adjacent measurements points.

The theoretical inter-planar spacing of the {311} plane is approximately 1.083 Å [32,63], giving a 2θ of 96.8° for the given wavelength. Asymmetry in the diffraction peak, consistent with recent work [32], was observed in this study. A background function was therefore generated and subtracted from the pattern to fit the {311} reflection of the parent NiCr γ phase only. This was necessary, as reflections of the coherent $Ni_3(Al,Ti,Nb)$ γ′ phase and Ni_3Nb γ′′ phase (a = 3.62 Å; c = 7.21 Å [65]) could overlap with and distort the parent γ peak [32,66]. This effect could be significant in aged IN718 which has a 10–15% volume fraction of γ′′ [65]. Also the {201} plane of the Laves phase, has a very similar d-spacing of 1.091 Å and could overlap [18], while the orthorhombic Ni_3Nb δ-phase cannot [65]. The Laves phase however are more likely to occur in as-deposited material [19]. The use of the background function also enabled determination of the full-width-half-maximum (FWHM) of the peak fit [67]. This procedure is elaborative, but necessary to improve the fit of the primary γ phase and other fit-values, such as the FWHM, as it can be seen with the example in Fig. 2 showing a very pronounced background.

The determination of the diffraction elastic constants (DEC) to correlate lattice strain with engineering stress is vital and not trivial. Wang et al. [41] performed an experiment to determine the DEC for as-deposited IN625, manufactured with blown-powder DED. The strong texture in the deposited nickel-alloy reduces the macroscopic stiffness significantly from E = 207 GPa of conventionally processed alloy to E = 152 GPa in additively manufactured IN625. The anisotropy in stiffness furthermore increases with increasing temperature. Also the specific lattice elastic constants for AM deposits are very different ($E_{311,AM}$ = 156.6 GPa), compared with wrought material ($E_{311,W}$ = 193.8 GPa) [41]. Aba-Perea et al. [10] measured the DEC for fine-grained and texture-free IN718 (E = 215 GPa; E_{311} = 201.7 GPa), which were not affected significantly after solution treatment and aging. Baufeld et al. [38] reported a very low macroscopic stiffness of E = 154 MPa in coarse-grained and textured WAAM-deposited IN718. Data from initial experiments [6,37] also suggest that wire composition and different stages of heat treatment do not influence the stiffness significantly. Inter-pass rolling however reduced texture and recovers the materials' stiffness. Based on all publications on this topic, several assumptions can be drawn to choose the DEC of the {311} plane with fair confidence. Since the stiffness seems to depend almost entirely on the texture, $E_{311,AM}$ = 156.6 GPa and ν_{311} = 0.31 [41] were chosen for both as-deposited specimen. The inter-pass rolled specimens with reduced texture were

Table 1
Chemical compositions (wt %) of the wire (AMS5832E) and substrate (HAYNES® 718 alloy) as per data sheet.

	Ni	Cr	Nb + Ta	Mo	Ti	Al	Co	Mn	Fe
Wire	53.15	19.42	5.22	2.95	0.96	0.47	0.41	0.11	Bal 17.3
Substrate	52 Bal	18	5	3	0.9	0.5	<1	<0.35	19

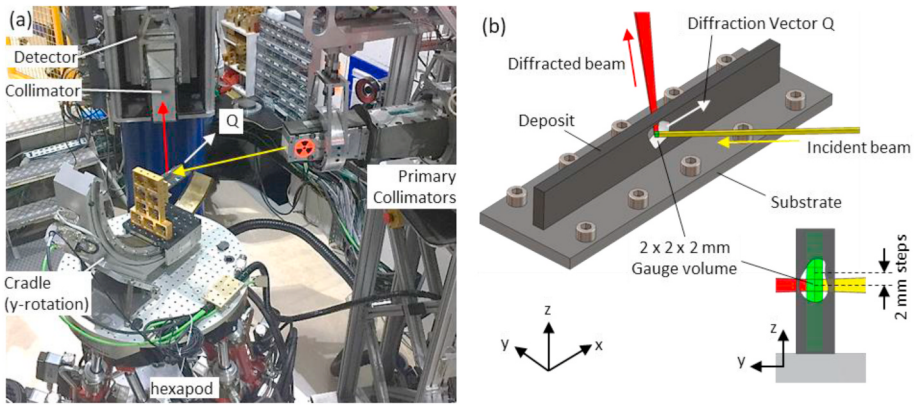

Fig. 1. a) setup of specimen on SALSA; b) location of gauge volumes and hardness plot line.

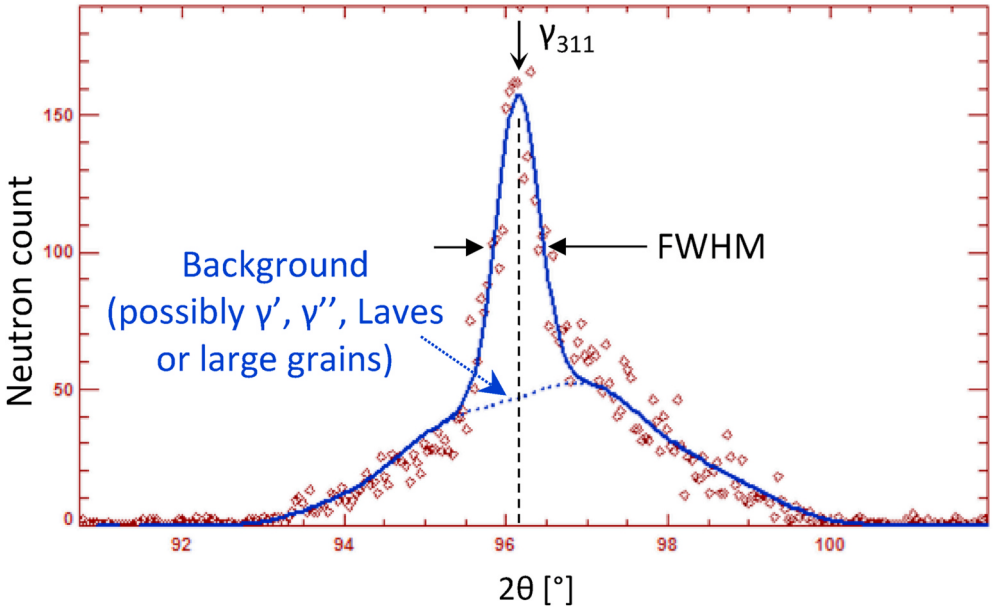

Fig. 2. Example of a fitted γ peak using a background function to compensate for potential disturbance sources.

calculated using the DEC $E_{311} = 201.7$ GPa and $\nu_{311} = 0.31$ [10]. This decision was only possible after the grain size was known from the EBSD data from this study.

The d-spacings of the {311} planes were calculated with Bragg's law (eq. (1)) and the lattice strain with eq. (2), directly with 2θ. The stress was finally analysed using Hooke's law (eq. (3)) using the individual DEC of the {311} plane. The fitting error of the diffraction angle 2θ propagates through the strain and stress calculation. Eq. (4) applied to determine the uncertainty of strain and stress yields eqs. (5) and (6) respectively. This does not take any of the other sources of error into account.

$$\lambda = 2d^{311} \sin\theta \tag{1}$$

$$\varepsilon_{ii}^{311}\left(d^{311}\right) = \left(\frac{\sin\theta_0}{\sin\theta}\right)_{ii} - 1 \tag{2}$$

$$\sigma_{ii} = \frac{\nu^{311}E^{311}}{(1+\nu^{311})(1-2\nu^{311})}\left(\varepsilon_{xx}+\varepsilon_{yy}+\varepsilon_{zz}\right) + \frac{E^{311}}{1+\nu^{311}}\varepsilon_{ii} \tag{3}$$

$$\Delta y = \sum_{i=1}^{n}\left|\frac{\partial f}{\partial x_i} * \Delta x_i\right| \tag{4}$$

$$\Delta\varepsilon_{ii} = \sqrt{\left(\frac{\cos\theta_0}{\sin\theta}\Delta\theta_0\right)^2 + \left(\frac{\sin\theta_0\cos\theta}{\sin^2\theta}\Delta\theta\right)^2}_{ii} \tag{5}$$

$$\Delta\sigma_{ii} = \frac{\upsilon E}{(1+\upsilon)(1-2\upsilon)}\left(\Delta\varepsilon_{xx}+\Delta\varepsilon_{yy}+\Delta\varepsilon_{zz}\right) + \frac{E}{1+\upsilon}\Delta\varepsilon_{ii} \tag{6}$$

2.3. Metallurgical preparation and microscopy

After the neutron diffraction experiment, the specimen was cut in the symmetry plane and mounted in conductive resin, representing the cross-section of the yz-plane of the neutron diffraction scan. The four specimens were ground and polished to 1 μm. For Scanning Electron Microscopy (SEM) and Electron Backscatter Diffraction (EBSD), specimens were given a final polishing with colloidal silica suspension. For optical microscopy, electrolytic etching for 10 s in 10% oxalic acid at 6 V revealed the microstructure. Vickers micro-hardness indentations were taken using a Zwick/Roell hardness tester at 0.5 kg load for 15 s. A ZEISS field emission gun SEM fitted with an Oxford Instruments Nordlys detector was used to conduct Energy Dispersive X-ray Spectroscopy (EDS) and EBSD, using acceleration voltages of 20 kV and 30 kV respectively.

3. Results and discussion

The effect of inter-pass rolling and SQA treatment on the microstructure and the consequent strength of IN718 WAAM structures was discussed in detail by Xu et al. [37], using a plasma heat source instead of CMT. The aim of the present work was to discuss the effect of the same processing route on residual stress and distortion, however some complementary aspects on the microstructure were found as well and are discussed beforehand, as they also help explaining the diffraction pattern during neutron diffraction.

3.1. Wall geometry and distortion

It took 9 passes to deposit the 6.89 mm wide and 2.39 mm high layers to build a wall larger than 21 mm. The as-deposited specimen is shown in Fig. 3 (a). With inter-pass rolling, each deposited layer was deformed, which decreased the height and increased the width, but the cross-sectional area was preserved. The bead-shape geometries, layer aspect ratio and the dilution for with and without rolled walls are shown in Table 2. It also shows that the CMT process resulted in the same level of dilution of 2 mm with the previous layer, regardless whether it was rolled before or not.

The distortion was quantified by measuring the out-of-plane distortion of the substrate [27], which has been done before on Ti–6Al–4V [23], mild steel [22] and aluminium 2319 [26] deposits using material-specific processing conditions, but comparable cross-sections. The distortion of the 180 mm long IN718 deposit (AD) was 3.61 ± 0.05 mm and of the IR specimen 0.99 ± 0.03 mm. To put this in context, Fig. 3 (b) compares the calculated curvature κ (= 1/R) of all four structural metals, which is independent from the length of the deposit. The cross-metal comparison will be discussed together with the residual stresses. Also shown is the distortion after inter-pass rolling using the highest load in the respective publications of the other structural metals.

3.2. Material and microstructure

The etched cross-sections of the as-deposited and the rolled wall are

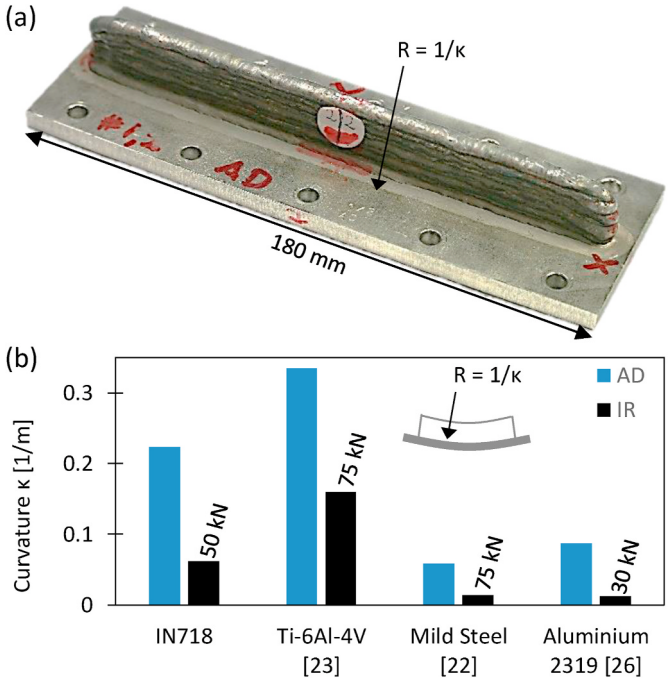

Fig. 3. Curvature of the distorted substrate after depositing 4 structural metals with WAAM with the same cross-sectional geometry [22,23,26].

Table 2
Cross-sectional geometries with and without inter-pass rolling.

	As-deposited	Inter-pass rolled
No. of layers	9	11
Total height [mm]	22.56 ± 0.11	20.91 ± 0.12
Layer height [mm]	2.39 ± 0.15	1.80 ± 0.12
Vert. Deformation ε_z [%]	–	−35.7 ± 0.9
Layer width [mm]	6.89 ± 0.24	8.01 ± 0.29
Transv. Deformation ε_y [%]	–	+11.2 ± 0.5
Layer aspect ratio	2.88	4.45
Dilution depth [mm]	~2	~2
Dilution [%]	~80	~110

shown in Fig. 4 (a) and (c) respectively together with a higher magnification for each (b, d). The dark dashed lines indicate the equidistant fusion boundaries. The white box indicates the location and dimension of the neutron diffraction gauge volume (NDGV). The top of the previous layer in the as-deposited wall is highlighted with the dashed line in Fig. 4 (a). At higher magnifications (Fig. 4 (b)) is becomes apparent that the large columnar dendrites grow through the fusion boundary, forming characteristic chain-pattern of the dark zones. Inter-pass rolling broke the dendritic growth through the layers, as shown in Fig. 4 (d) and the dark zones appear finer and more equiaxed. In the as-deposited microstructure, a few rare deposition defects can be identified. A representative gas pore and a lack-of-fusion defect is shown in Fig. 5 (a) and (b) respectively. The inter-pass rolled specimen was less populated with visible pores. Laves phase were observed between the dendritic columns of the parent γ matrix, as shown in Fig. 5. This microstructure is typical of IN718 DED [20], which can result from high heat inputs and slow cooling rates causing segregation of heavier elements into the inter-dendritic region [68]. Smaller equiaxed grains interrupting the dendritic columns were also found in the microstructure, as illustrated by the marked grain boundaries in Fig. 5.

In general the FWHM can be influenced by several factors, of which one is plastic deformation. The FWHM plot in Fig. 6 (a) shows virtually constant values along the height of each deposit, with one exception. The IR-specimen, which was the only specimen that has been rolled as last step, shows increased values approximately in the top 4–5 mm of the wall.

This increase in FWHM near the top is mainly due to plastic deformation [69], which is supported by the hardness plot of the IR specimen in Fig. 6 (b), showing work hardening to the same depth. This is approximately the depth of the layer height (~2 mm) plus the dilution depth (~2 mm) of the previous layer combined (Table 1). Half of the cold worked material was remelted during deposition of the subsequent layer, however the cold worked region below that was not. Instead it experienced a thermal cycle by the process heat of the next deposition. The resulting hardness is with overall >360 HV, significantly improved when compared to the as-deposited hardness in specimen #1 of 247 ± 7 HV, which practically constant along the height. SQA heat treatment of both conditions further increased the hardness. The unrolled specimen has an overall hardness of 427 ± 9 HV, while the rolled specimen even reached 441 ± 7 HV after SQA and both are fairly constant along the height as well. The overall hardness profiles are in-line with previous work [37]. However in the present study a denser hardness scanning were performed. The necessity in doing that in AM parts becomes apparent from Fig. 6 (b), as the experimental scatter can exceed the effect of processing conditions and deviations within a single layer, which, with a larger number of measured points, can be statistically normalised by using a larger number of parallel indents and a smaller step distance.

The large columnar grain structure observed in the optical micrographs of Fig. 4 (a) was also observed in the EBSD maps of the as-deposited SQA material, as shown in Fig. 7. The grain size ranges from 50 to 500 μm in thickness and are several mm long in the build direction. The map follows an inverse pole figure (IPF) colouring referenced to the

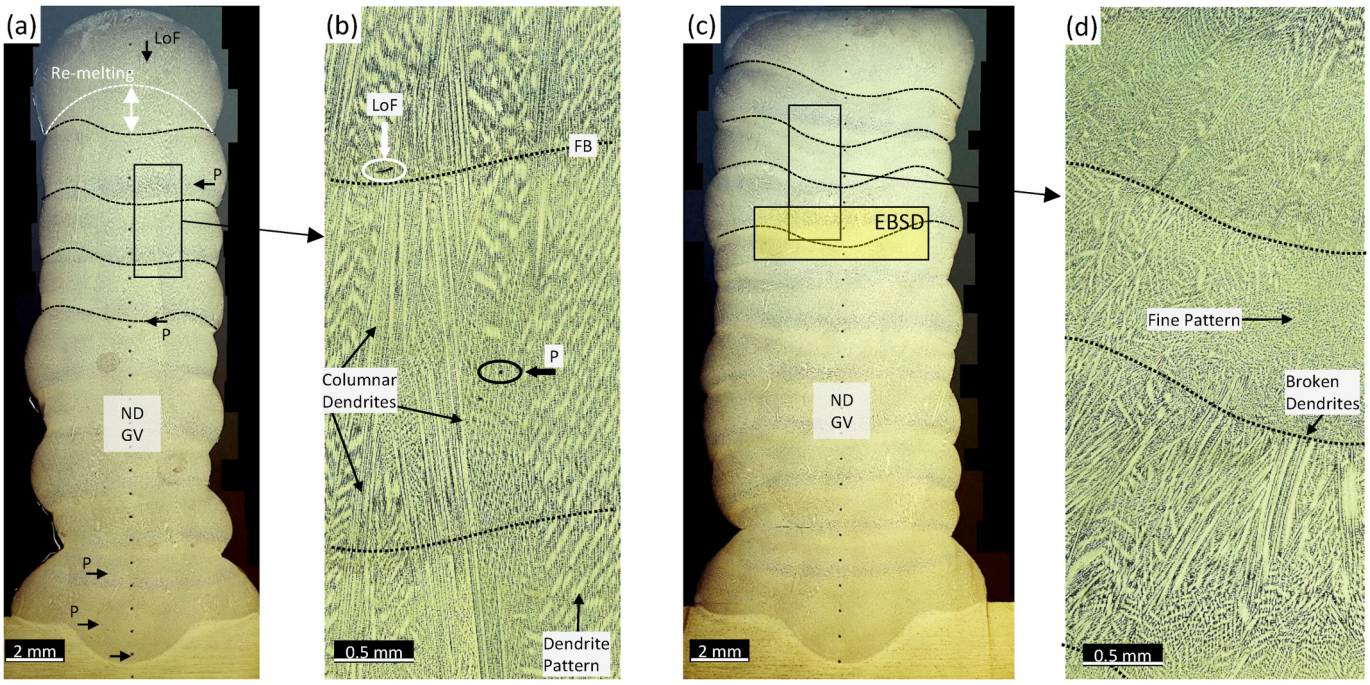

Fig. 4. (a, b) as-deposited and (c, d) inter-pass rolled microstructure with magnification showing characteristic features: lack of fusion (LoF) defects and pores (P) (see Fig. 5 for more detail), fusion boundaries (FB), Laves phase (dark) surrounding the columnar γ dendrites; location and scale of a neutron diffraction gauge volume (NDGV).

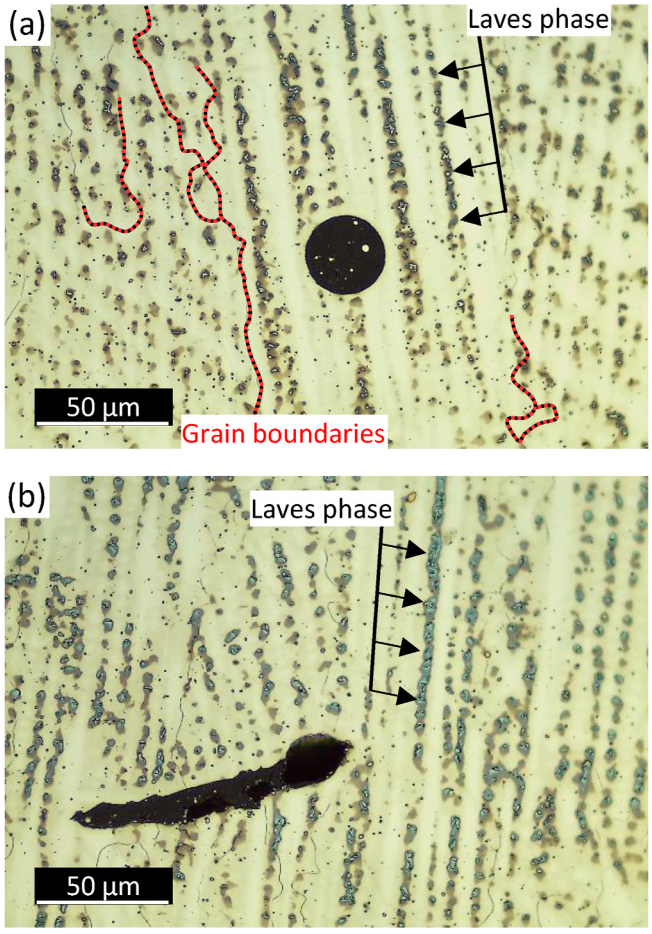

Fig. 5. rare (a) gas pore and (b) lack of fusion defects from Fig. 4 (b), with grain boundaries and long-chained Laves phase dendrites.

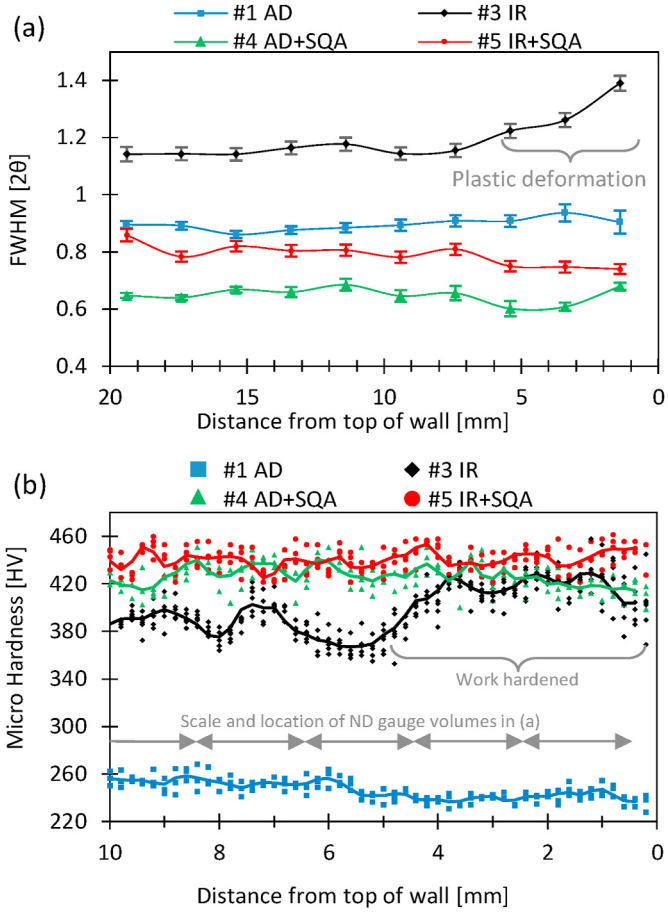

Fig. 6. (a) FWHM of the neutron diffraction measurement and (b) hardness measurements plus averaged trendline near the top of the deposits. The labels refer to the microstructure in the IR specimen (Note the dissimilar x-scale).

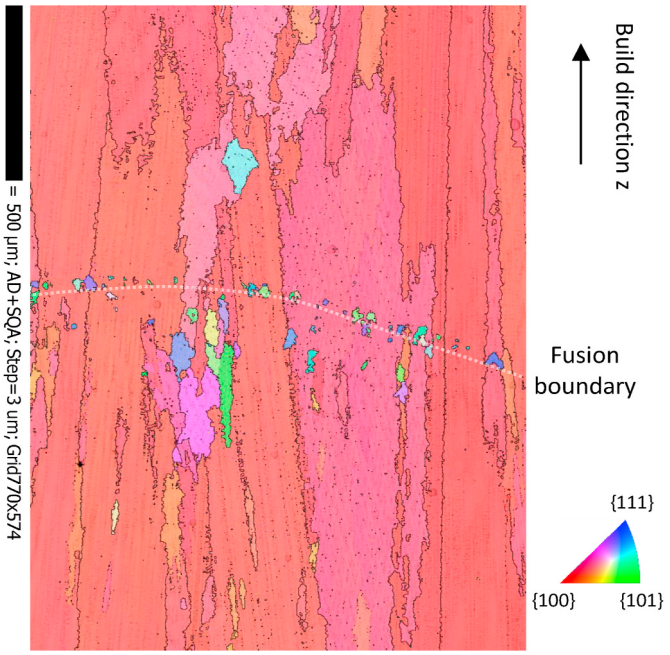

Fig. 7. IPF-z EBSD map overlapped with band contrast scan of the as-deposited + SQA deposit.

build direction z. The map shows strong texture, where the grains are well oriented in the preferred growth direction <001>, parallel to the build direction (z) of the WAAM part. This texture is responsible for the anisotropic mechanical properties [37] and can also be found in other metal systems, such as titanium [70]. The band contrast overlay in Fig. 7 shows the dendritic stems with growth in line with the elongated axis of the grains. The map also shows several small grains amongst the large columnar ones. Their misorientation suggests that they might have nucleated during deposition but were outgrown by the surrounding columnar neighbours. A chain of small misoriented grains populated along the fusion boundary and highlight the epitaxial growth of the surrounding grains.

Large area EBSD maps of the inter-pass rolled materials (with and without SQA) in Fig. 8 (a) and (b) respectively show that inter-pass rolling causes grain refinement and reduction in texture. Non-uniformity in the effects of rolling, was observed in the EBSD map of the IR sample without SQA shown in Fig. 8 (a). This alternating band of fully and partially recrystallised areas, was observed in a previous studies with mild steel [22] and In718 [37]. The fine equiaxed grains have an average grain size of 11.4 ± 6.3 µm, while the larger grains have a circle equivalent diameter of 118.2 ± 2.8 µm. Zhang et al. [71] described the effect of plastic strain and holding times after hot forging at 980 °C on the resulting grain size. 10% compressive strain was the minimum to achieve a final grain diameter below 70 µm, while 40% and more could further decrease the diameter to <50 µm at shorter holding times. Admittedly the hot forming process is not necessarily comparable to the cold rolling, however subsequent grain growth during holding should be comparable. In comparison with the literature [72], the present grain size is slightly smaller, possibly suggesting that the solution treatment temperature may have been slightly lower. The equations of Ruan et al. [73] can furthermore be used to predict the grain diameter during subsequent growth at high temperatures.

However, the misorientation map of the IR specimen in Fig. 8 (c) suggests plastic deformation inside the crystal, especially in the coarse grained region, triggering the refinement during SQA treatment. The misorientations fully recovered during SQA treatment (Fig. 8 (d)) and resulted in the fully recrystallised microstructure Fig. 8 (b)).

The texture of the material was significantly improved after inter-pass rolling, as observed in several structural metals deposited using WAAM [22,37,70]. The pole figures Fig. 9 quantify the randomisation of textureacross the AD SQA map (Fig. 7), IR and IR + SQA samples (Fig. 8 a, b). Fig. 9 (a) shows the strongest intensity of 22.19 for the {100} family of grains oriented along the transverse direction, in line with the red colouring in Fig. 7. Fig. 9 (b) and (c) show much lower intensities of 3.47 and 1.73 respectively, indicating a significant randomisation of texture caused by inter-pass rolling. SQA treatment of the IR deposit further reduced the texture, as also the coarser grains were refined during the solution treatment, allowing recrystallisation of the coarser grains that contained stored strain energy in form of dislocations induced by rolling.

The materials strength is not only affected by texture and grain size, but principally by the quantity and distribution of γ". The precipitation of γ" during aging requires Nb to be dissolved in the parent γ matrix after solution treatment. The contrast of a BSD image can be influenced by both sample topography and elemental differences [74]. Island-like phases were observed in the SEM backscatter electron detector (BSD) image of the AD specimen without SQA, shown in Fig. 10 (a). These phases are not topographically artefacts, but the inter-dendritic secondary phases also observed using optical microscopy (Fig. 5), which was confirmed with secondary electron images during the analysis. The EDS maps shown in Fig. 10 (b) and (c) highlight the areas which are high in Nb and Ti respectively. The Nb map confirms that the lighter areas of Fig. 10 (a) are rich in Nb. The morphology of the phase and its corresponding richness in Nb suggests that the island-like precipitates observed are undesired Laves phase. Embedded in the Laves phase, as pointed out by the blue arrow in Fig. 10 (a), is a dark spot which is rich in Ti. Whilst the composition of the particle has not been confirmed in this study, similar particles have been found elsewhere [6,37], suggesting that these are TiN particles what can be traced back to the wire feedstock of IN718 WAAM. TiN acts as nucleation sites for carbides such as NbC [75] which can be detrimental for mechanical properties. Upon comparison with the Ti map shown in Fig. 10 (c), it becomes apparent that not all the dark spots in the electron image are Ti-rich particles and some of them are likely to be micropores instead.

Fig. 10 (d) shows the BSD image of the AD specimen after SQA treatment, showing needle-like phase surrounding the Laves phase. These features are too fine to be resolved in the EDS maps but are likely to be δ phase. Fig. 10 (e) shows that a slight increase in Nb concentration can be found in the δ phase, but a large quantity is still locked away in the Laves (red arrows) and δ (yellow arrows), which reduces the amount of Nb available for the precipitation of γ'', limiting the aging response of the material [37]. Laves remains in the microstructure as the solution treatment temperature applied is lower than the dissolution temperature of Laves, which is around 1200 °C [76]. The Ti map in Fig. 10 (f) has also spots with higher concentration (blue arrows) easily to be mistaken for micropores in the BSD image (a), which is consistent with those observed in Fig. 10 (c).

3.3. Neutron diffraction

The plot of the stress-free reference along the height of each specimen and orientation is shown in Fig. 11. No clear trends can be observed within any of the profiles, however large deviations along the height are visible especially in both samples without rolling (a, c). The largest deviation can be found in the normal z-direction of the AD specimen (a). This error in d_0 alone would already translate into pseudo microstrain and later in an error in calculated stress of ±100 MPa. No conclusive trend can be drawn from the d_0 profiles of the unrolled specimen that could be correlated to the processing and can only be due to larger grain size and orientation, which would have insufficient statistics. The inconsistency in Fig. 11 illustrates the difficulties of determining a representative d_0 reference in neutron diffraction in textured and coarse-grained material. This is due to the large grain size (Fig. 7) and strong texture (Fig. 9 a) in the unrolled walls, leading to a smaller

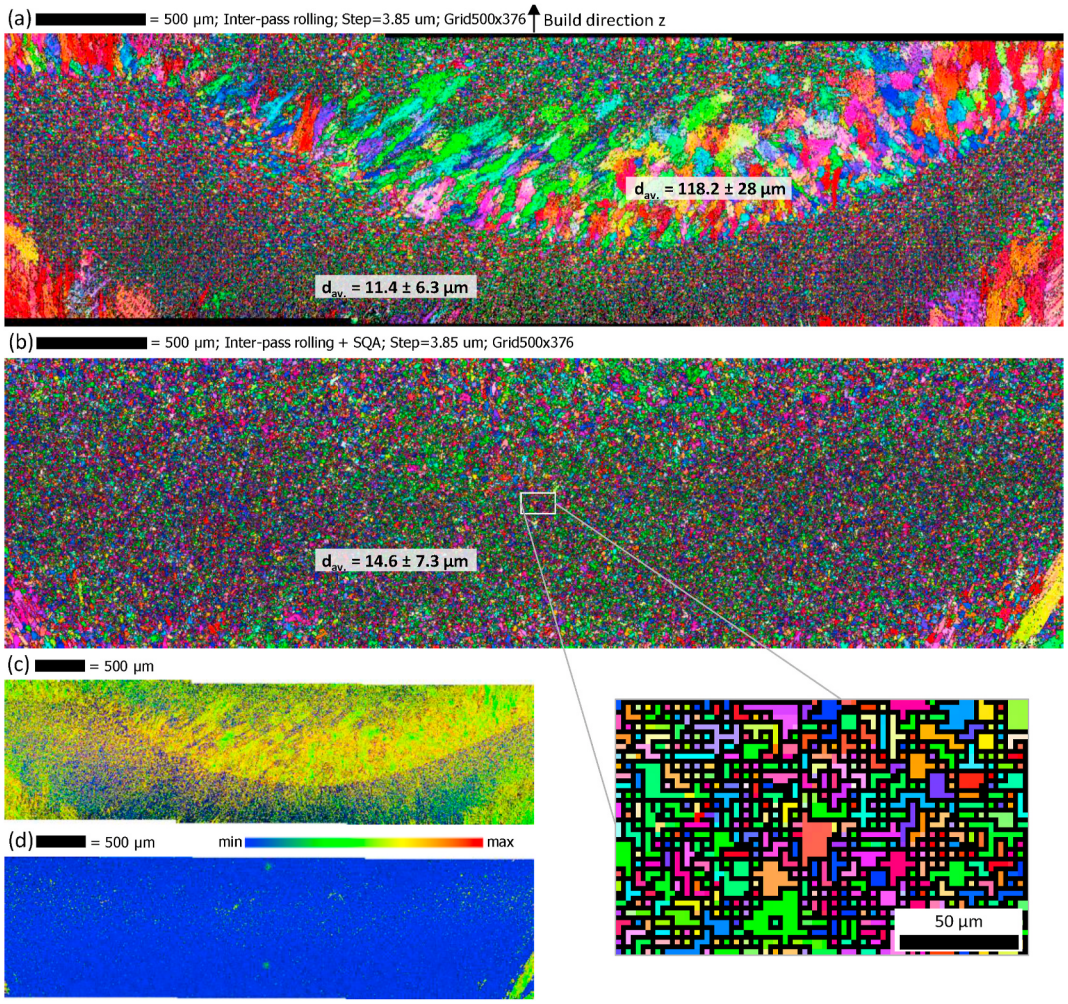

Fig. 8. IPF-z EBSD maps, local average grain size d_{av} and Vickers micro hardness h_{HV} in the (a) inter-pass rolled wall and the (b) inter-pass rolled wall + SQA treatment. Grain size, and hardness are taken from the centre map. The misorientation maps (c) and (d) correspond to (a) and (b) respectively.

number of scattering crystallites in the gauge volume and less representative d_0 samples. The rolled walls have a much smaller grain size (Fig. 8) and very little texture (Fig. 9 b, c), which would ensure better statistics to capture macrostrain variation. It is however noteworthy that the macrostrain difference between different processing routes is less than previous reported work using the over-saturated aluminium-copper alloy 2319 [26].

The lattice strains of the {311} plane in the five specimens along the vertical centre line are shown in Fig. 12(a–e) with identical scale. The error bars indicating the calculated error based on the peak fit accuracy, with an average of less than 55 microstrain. The as-deposited specimen (a) shows the largest tensile strains in the clamped condition between 2000 and 3000 microstrain in the longitudinal direction. It also shows the largest compressive strains up to −2000 microstrain in normal direction, while the transverse strain is relatively low. Large and consistent compressive transverse strain can be found in both inter-pass rolled specimen (c) and (e).

Fig. 13 shows the calculated residual stresses in the five specimens. The longitudinal yield strength of WAAM deposited IN718 is 525 ± 7 MPa [37], indicated with a dashed line in Fig. 13 (a). The longitudinal process residual stresses reach this value, while the transverse and normal stresses are lower. Thiede et al. [33] reported cyclic thermal relaxation of previous layers in Selective Laser Melting of IN718, which determines the peak tensile stresses in the bulk material. Constant longitudinal residual stresses are common in WAAM and responsible for the bending distortion [21–27,77]. The stress reported by Smetannikov et al. [36], who used a similar deposition process, were lower. One reason is that the 10 layers were deposited with little waiting time, causing the substrate to heat up above 350 °C during deposition, which reduced the mismatch of thermal strain and therefore developed less residual stress. Another reason is that they did not account for potential phase transformation stress. A controlled and elevated substrate temperature is therefore a possible solution to significantly reduce residual stress and distortion in IN718 WAAM and other alloys.

The residual stresses redistribute in Fig. 13 (b) after unclamping, but show identical characteristic point-to-point pattern and local trends, such as the distinct drops 12 mm above the substrate. The longitudinal stress drops significantly to less than 250 MPa due to distortion [27], while the two components in transverse and normal direction remain fairly constant compared to the clamped condition. The other two stress components hardly change at all, as the part mainly distorts around the y-axis, which is comparable to other deposited structural metals [22–24, 26].

The residual stresses in IN718 WAAM can be with 500 MPa as high as the ones in Ti–6Al–4V [23–25]. Fig. 3 however shows that the distortion is less, which is due to the higher stiffness of 200 GPa in the nickel-based alloy, as opposed to 113 GPa of titanium, yielding in more elastic residual strain in the latter. However the distortion is still much more severe compared with mild steel [22] and aluminium [26], which can also be respectively explained by the individual residual stress to stiffness ratio.

The established longitudinal process residual stress in the bulk of the

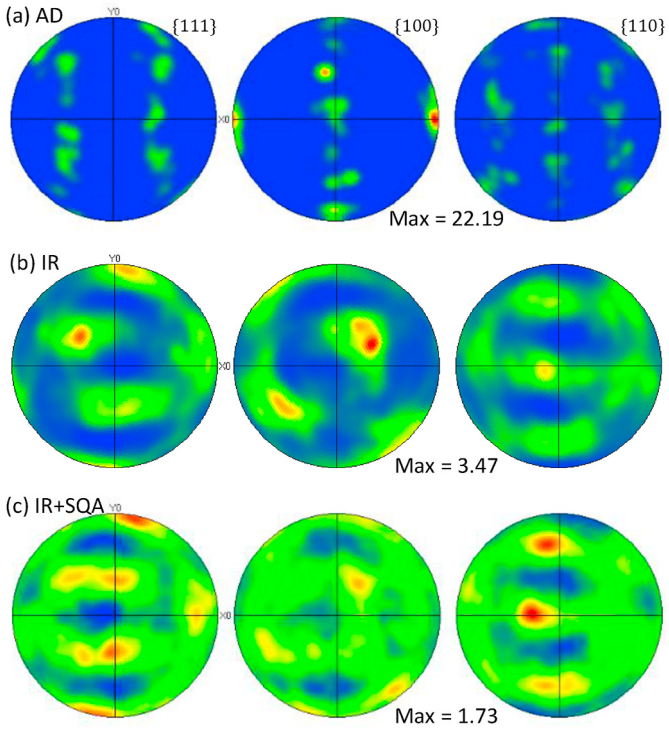

Fig. 9. Pole figures showing the texture of (a) as-deposited WAAM deposition of IN718 and the effect of (b) inter-pass rolling and (c) inter-pass rolling + SQA.

wall are around 300 MPa, apart from the area near the substrate and the top region that was rolled in the last step (Fig. 13 c). It was previously suggested that rolling deforms each layer in such a way that these tensile stresses in the bulk wall are balanced by compressive stresses on both side surfaces of the wall [26]. The transverse and normal stresses appear lower than the longitudinal stress, but all three components align and show a significant drop due to the last rolling action, inducing compressive stresses up to −300 MPa and affect the material approximately 5 mm below the top surface. This depth is in-line with the FWHM, as well as the hardness profiles in Fig. 6 (a) and (b) respectively. Fig. 3 shows furthermore that rolling is capable of reducing residual stress and distortion in mild steel and aluminium WAAM, while this is not the case for Ti–6Al–4V at the maximum rolling loads for the respective metal. In IN718 a reasonable reduction in residual distortion can be achieved with 50 kN rolling load on a 7 mm wide wall. However higher loads (e.g. 75 kN) are possible [37], which is expected to further reduce residual stress and distortion.

Solution treatment, quenching and aging can increase the yield strength of as-deposited IN718 to 790 MPa without rolling and above 1000 MPa with rolling, as rolling refines the grains, and promotes the aging response of the alloy, by better distributing the Nb [37]. As-deposited single pass walls typically do not show stress gradients through the thickness of the wall [23,24]. Inter-pass rolling and can cause compressive stress on the surface and tensile stresses in the bulk of a WAAM deposit [26]. The subsequent solution treatment at 975 °C for 1 h however relieve most of the stresses, but they can be re-introduced by quenching [11]. The stresses of the SQA specimen in Fig. 13 (d) and (e) are therefore likely to be due to the SQA treatment, rather than the deposition. However a stress measurement in solutionised and solutionised and quenched conditions are required to be certain. The profile of the AD + SQA sample oscillates around zero stress, suggesting low residual stresses, however the scatter in the data is high. The confidence in the measurement of the IR and IR + SQA specimen is higher. It shows zero stress in normal direction and little tensile stresses in longitudinal direction that increase near the interface with the substrate. Dye et al. [11] reported longitudinal (hoop) tensile stresses in the bulk of an IN718 quenched disk up to 400 MPa that are balanced by surface compressive stress. This stress field is caused by the transient thermal field during quenching [11] and is also expected to have induced balancing compressive stress at the side-surface of the wall. The subsequent aging heat treatment was performed at 718 °C for 8 h and is not expected to have modified the stress state subsequently [7,43].

The ND investigation of this WAAM-built Inconel is challenging, due to several aspects. Additive Manufacturing often produces large columnar grains with strong texture and the chemical composition is highly sensitive to the thermal history. It is therefore possible that an analogous reference specimen does not have identical morphology, crystal orientations and composition as the specimen to be investigated. Stress-free references from the actual specimen after it was measured would be needed for a representative reference d_0, which is not practical with consecutive instrument time, as the EDM cuts need to be performed within the experimental time. The weakness in the measurement is not

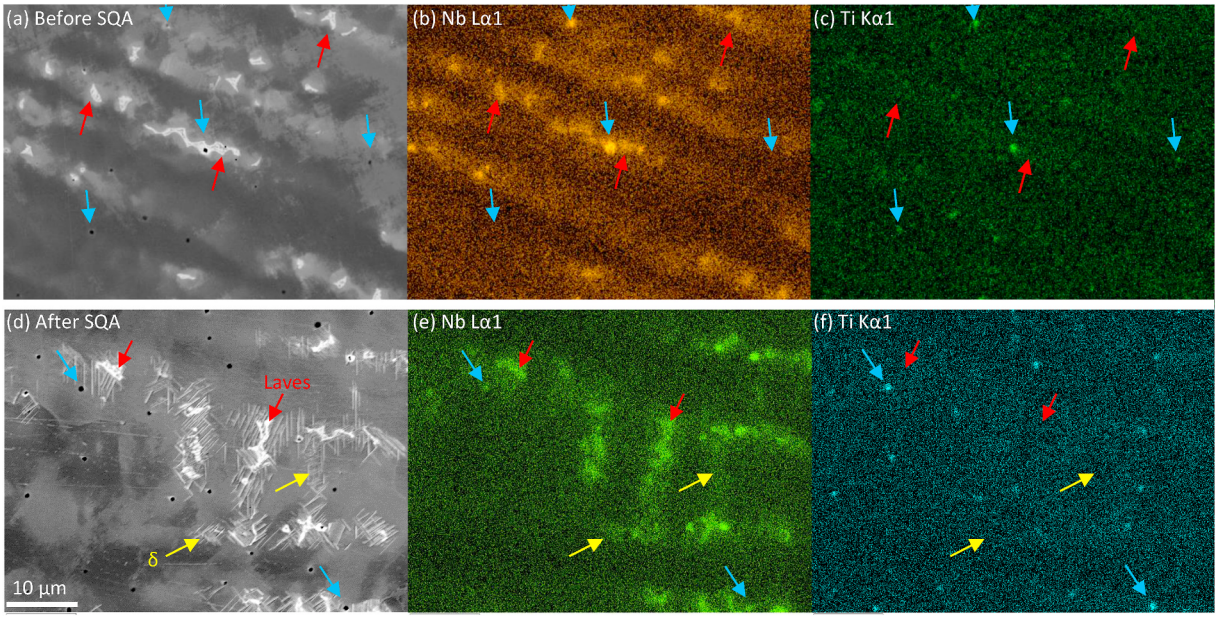

Fig. 10. WAAM-deposited IN718 without (a–c) and with (d–e) SQA: (a, d) SEM-BSD image and EDS elemental maps of (b, e) Niobium and (c, f) Titanium.

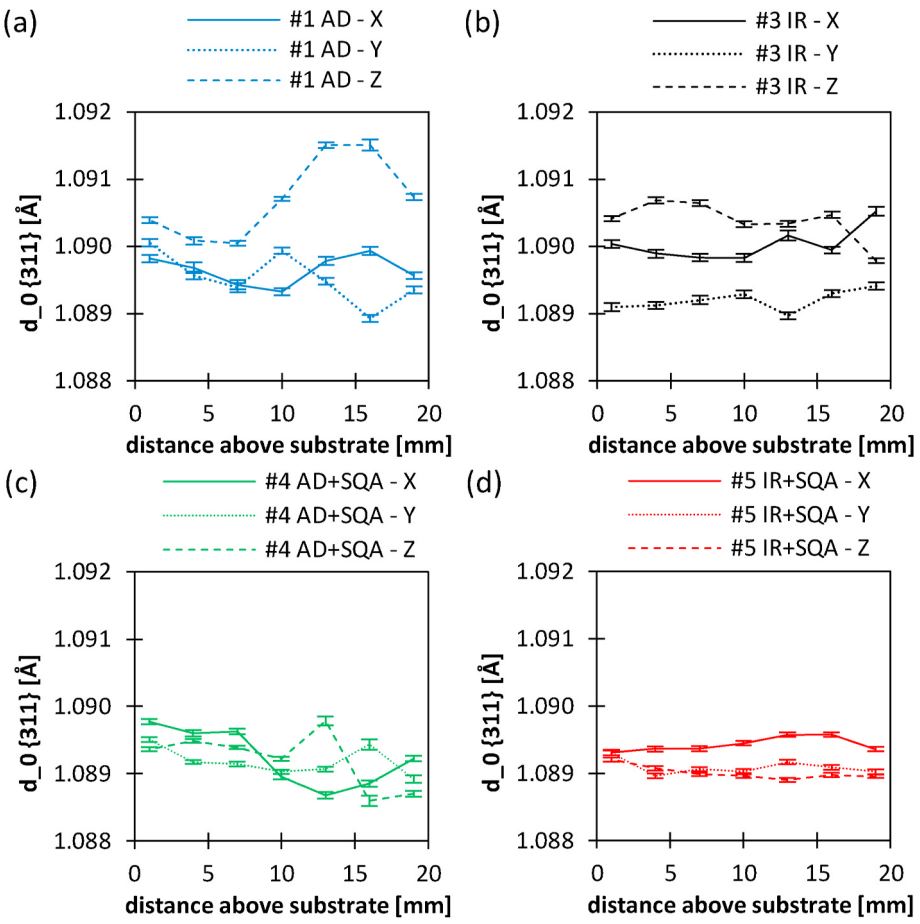

Fig. 11. d_0 reference lattice profiles of the {311} plane in the three directions in the (a) as-deposited wall, (b) the inter-pass rolled wall and (c, d) the respective walls after SQA treatment.

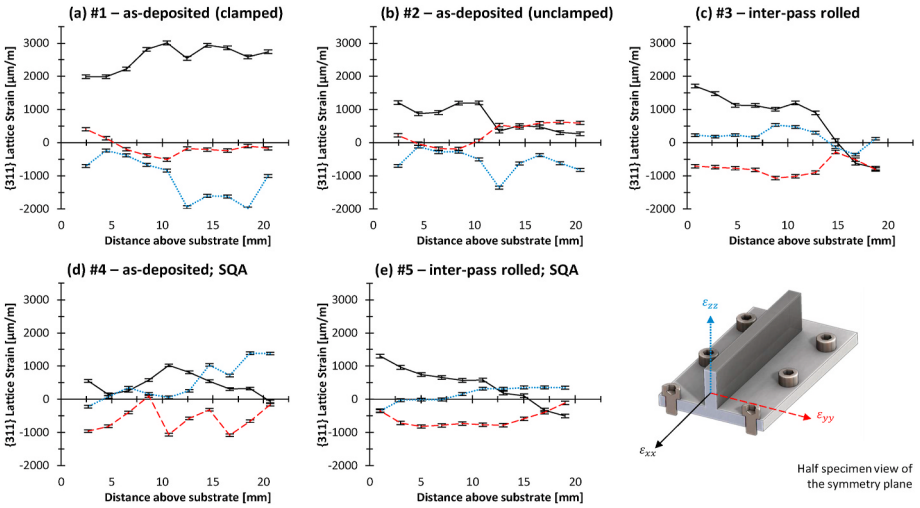

Fig. 12. {311} lattice strain in the three principal directions in the deposit of (a) the as-deposited control specimen before and (b) after unclamping; (c) the inter-pass rolled specimen; (d) and (e) the solution treated, quenched and aged version of (b) and (c).

the method of neutron diffraction, but the limited reproducibility of microstructure in WAAM. In nickel superalloys it should also be considered to measure the DEC for the specific specimen, which however uses a large share of the total beam time, making the experiment inefficient. A fair compromise was therefore allowing for larger errors and perhaps comparing the measurement with other non-diffraction techniques, such as the contour method [23–25]. Inter-pass rolling is known to improve the microstructure and the response to heat treatment [37,58]. A beneficial side-effect is also the improved diffraction quality due to smaller grains and the reduced texture [25], which was also observed in the present experiment. The compensation with a background (Fig. 2) function was needed to account for random asymmetry due to secondary phases. Rietveld refinement of the whole diffraction pattern using energy-dispersive neutron sources, covering several peaks

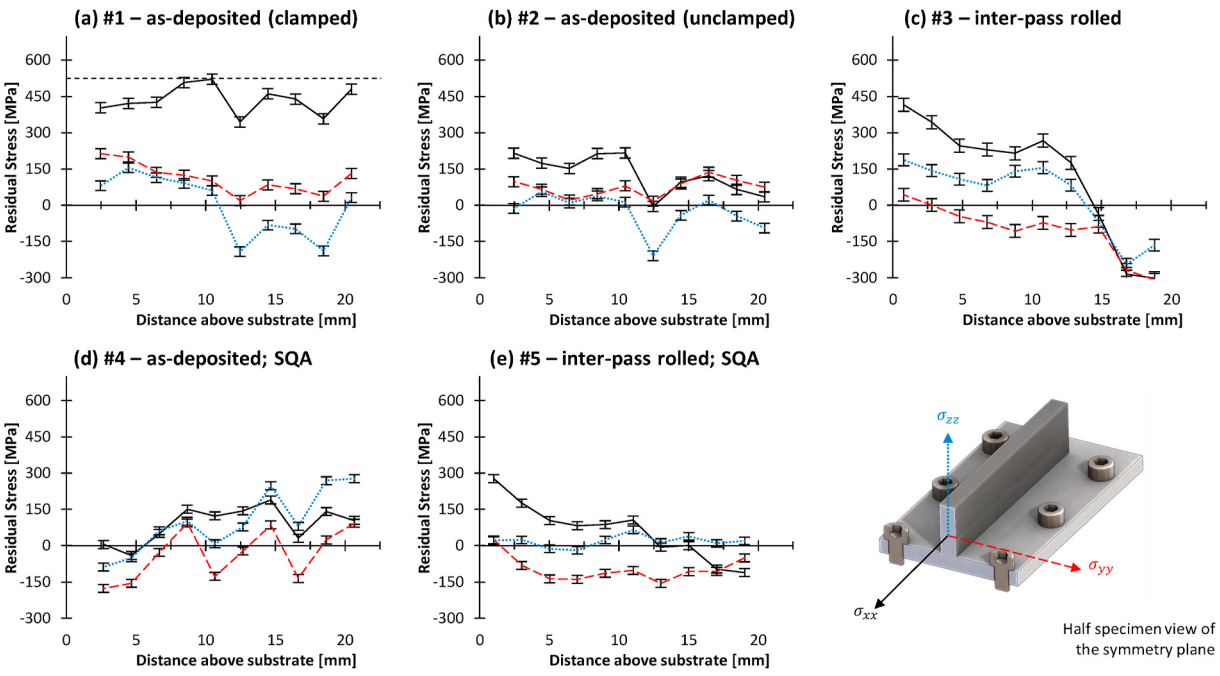

Fig. 13. Calculated residual stress in the three principal directions in the deposit of (a) the as-deposited control specimen before and (b) after unclamping; (c) the inter-pass rolled specimen; (d) and (e) the solution treated, quenched and aged version of (b) and (c). The horizontal dashed line in (a) indicates the longitudinal yield strength [37].

at once, can be an alternative that mitigate the issues of overlapping peaks of second phases [11]. This would however require longer counting times. Figs. 12 and 13 show the strain and residual stress profiles respectively. The poor point-to-point consistency in both of the AD specimen before and after unclamping (#1 and #2 respectively) and AD + SQA (#4) suggest material-related intricacies compared to the good consistency in the IR specimen without and with SQA treatment (#3 and #5 respectively).

3.4. General discussion

Different DED heat sources, such as laser [20], plasma arcs [37] or CMT [6], can be used to deposit IN718 alloy. However the layer-by-layer processes typically generate large columnar grains with a strong texture and the finite cooling rates during solidification promote the precipitation of Nb-rich Laves phase, which prevent the material from reaching the desired strength during the SQA treatment. A lot of effort is made to overcome this issues, for example by using special laser modes [20], which is not possible in WAAM. Inter-pass rolling is currently the only way of depositing this nickel superalloy at high deposition rates with a microstructure that reaches excellent material properties [37]. Another advantageous side-effect of rolling are significantly reduced residual stresses and part distortion during the manufacture. This makes the clamping, part manipulation and subsequent heat treatment much more manageable and reduces the risk of build failures significantly. The downside of rolling is of course that it limits the free-form capability of additive processes. However, part complexity and topology [78] optimisation are not the business driver of WAAM anyway. Typical WAAM applications are the 1-to-1 replacement of existing parts that are conventionally manufactured by casting, forging and machining from solid with the advantage of reducing lead-time and the buy-to-fly ration [1]. The complexity of these manufacturing techniques is manageable, hence rolling does limit WAAM substantially. Most geometries that are in the scope of the technology are compatible with rolling.

4. Conclusion

Inter-pass rolling has several benefits. In addition the positive effect on microstructure and mechanical properties [37], this study has furthermore revealed other advantages.

1. As-deposited WAAM deposition of IN718 produced large columnar grains with strong texture. During eutectic solidification interdendritic Laves phases form in long chains. The high local concentration of Niobium in the Laves phase cannot be re-dissolved during solution treatment. However inter-pass rolling can mitigates the problem and furthermore produces a very fine microstructure with virtually eliminated texture.
2. After inter-pass rolling the microstructure shows alternating regions of very fine equiaxed grains with little texture and regions of slightly columnar and more textured grains. When SQA treated, the slightly coarser region appears to refine as well. More detailed work is needed to better understand the effect of plastic strain and thermal history on the resulting microstructure.
3. Residual stresses in IN718 WAAM can exceed 500 MPa and result in significant part distortion. Inter-pass rolling can reduce both significantly. Hardness and FWHM profiles agree well with the penetration depth of the induced residual stress. The results also suggest that tensile residual stresses in the bulk material must be balanced by compressive stress on the side surfaces. However surface waviness of the rolled specimen complicates the stress measurement in this area using diffraction or destructive techniques.
4. Large grains and strong texture of additively manufactured IN718 can increase the risk of not producing representative stress-free reference specimen for neutron diffraction. Radial collimators, oscillation of the diffraction vector and background functions can be used to mitigate effects. Refining the microstructure and reducing the texture by inter-pass rolling is not only beneficial for the mechanical properties, but it also enhances the diffraction characterization of such components with appropriate spatial resolution.
5. Defects, such as gas-pores or lack of fusion, can occur occasionally in IN718 using CMT heat sources for WAAM. Inter-pass rolling appears

to mitigate the risk of porosity, however their detrimental effect on dynamic mechanical properties has to be quantified.

6. EDS maps suggest the presence of TiN particles, which are likely to originate from the wire feedstock. Rolling did not influence the quantity. It is not known whether these particles effect the mechanical performance of WAAM components.

CRediT authorship contribution statement

Jan Hönnige: Main author of the paper. Jan did planning of all the experiments, developed the wire plus arc additive manufactured samples and participated in the neutron diffraction experimentation. **Cui Er Seow:** Performed all the advanced characterisation of the WAAM built samples under different processing conditions and participated in discussions for correlation of processing condition to the microstructural characterisation and hardness. **Supriyo Ganguly:** Supervision, Writing - original draft, Supervisor of Xiangfang Xu and subject advisor to Jan Hönnige. Supriyo participated in writing for the beam time application, in planning experiments, participation in the neutron diffraction experiment at ILL and contribution to the manuscript. He is also the corresponding author. **Xiangfang Xu:** Writing - original draft, Participated in neutron diffraction experiments, helped during building of WAAM structure and contributed towards discussions during preparation of the manuscript. **Sandra Cabeza:** Formal analysis, Sandra is the instrument scientist at SALSA, ILL. She helped us as the Instrument scientist during the experimentation. She also helped in analysis of data from the neutron diffraction experimentation. **Harry Coules:** Supervision, Formal analysis, Writing - original draft, Harry was the supervisor of Cui. Harry helped in the microstructural analysis part during preparation of the manuscript. **Stewart Williams:** Supervision, Writing - original draft, Stewart is the PI of the NEWAM programme. He was also supervisor of Jan Hönnige and helped in improving the technical discussion part of the manuscript particularly the redistribution of residual stress and distortion part of the manuscript.

Declaration of competing interest

The authors declare that they have no known competing financial interests or personal relationships that could have appeared to influence the work reported in this paper.

Acknowledgement

The authors would like to give their gratitude to Flemming Nielsen from Cranfield University, Peter Ledgard from The Open University, Milton Keynes, and Thilo Pirling from the SALSA beamline at ILL. The financial support was given through the New Wire Additive Manufacturing (NEWAM) project by the Engineering and Physical Sciences Research Council (EPSRC) (Project number - EP/R027218/1).

Appendix A. Supplementary data

Supplementary data to this article can be found online at https://doi.org/10.1016/j.msea.2020.140368.

References

[1] S.W. Williams, F. Martina, a.C. Addison, J. Ding, G. Pardal, P. Colegrove, Wire+arc additive manufacturing, Mater. Sci. Technol. 32 (7) (2015) 641–647.
[2] A. Ugarte, R.M. Saoubi, A. Garay, P.J. Arrazola, Machining behaviour of Ti-6Al-4V and Ti-5553 alloys in interrupted cutting with PVD coated cemented carbide, in: *5th CIRP Conference On High Performance Cutting* 2012 vol. 1, 2012, pp. 202–207.
[3] C.P. Kuo, S.C. Su, S.H. Chen, Tool life and surface integrity when milling inconel 718 with coated cemented carbide tools, J. Chinese Inst. Eng. Trans. Chinese Inst. Eng. A/Chung-kuo K. Ch'eng Hsuch K'an 33 (6) (2010) 915–922.
[4] D. Clark, M.R. Bache, M.T. Whittaker, Shaped metal deposition of a nickel alloy for aero engine applications, J. Mater. Process. Technol. 203 (1–3) (2008) 439–448.
[5] D. Clark, M.R. Bache, M.T. Whittaker, Microstructural characterization of a polycrystalline nickel-based superalloy processed via tungsten-intert-gas-shaped metal deposition, Metall. Mater. Trans. B Process Metall. Mater. Process. Sci. 41 (6) (2010) 1346–1353.
[6] X. Xu, J. Ding, S. Ganguly, S. Williams, Investigation of process factors affecting mechanical properties of INCONEL 718 superalloy in wire + arc additive manufacture process, J. Mater. Process. Technol. 265 (2019) 201–209.
[7] Z. Wang, A.D. Stoica, D. Ma, A.M. Beese, Stress relaxation in a nickel-base superalloy at elevated temperatures with in situ neutron di ff raction characterization - application to AM, Mater. Sci. Eng. A 714 (2018) 75–83.
[8] A. Thomas, M. El-Wahabi, J.M. Cabrera, J.M. Prado, High temperature deformation of Inconel 718, J. Mater. Process. Technol. 177 (1–3) (2006) 469–472.
[9] C.M. Kuo, Y.T. Yang, H.Y. Bor, C.N. Wei, C.C. Tai, Aging effects on the microstructure and creep behavior of Inconel 718 superalloy, Mater. Sci. Eng. A 510–511 (2009) 289–294.
[10] P.E. Aba-Perea, T. Pirling, P.J. Withers, J. Kelleher, S. Kabra, M. Preuss, Determination of the high temperature elastic properties and diffraction elastic constants of Ni-base superalloys, Mater. Des. 89 (2016) 856–863.
[11] D. Dye, B.A. Roder, S. Tin, M.A. Rist, J.A. James, M.R. Daymond, Modeling and measurement of residual stresses in a forged IN718 superalloy disc, Miner. Met. Mater. Soc. (2004) 315–322, no. Superalloys.
[12] A.M. Korsunsky, G.M. Regino, D.P. Latham, H.Y. Li, M.J. Walsh, Residual stresses in rolled and machined nickel alloy plates: Synchrotron X-ray diffraction measurement and three-dimensional eigenstrain analysis, J. Strain Anal. Eng. Des. 42 (2007) 1–12.
[13] J.M. Oblak, D.F. Paulonis, D.S. Duvall, Postprocessed-tle catalogue for conjunction detection with geo passive objects, Metall. Trans. 5 (1974) 143–153.
[14] D.F. Paulonis, J.M. Oblak, D.S. Duvall, PRECIPITATION IN NICKEL-BASE ALLOY 718, 1969.
[15] G. Appa Rao, M. Kumar, M. Srinivas, D.S. Sarma, Effect of standard heat treatment on the microstructure and mechanical properties of hot isostatically pressed superalloy inconel 718, Mater. Sci. Eng. A 355 (2003) 114–125.
[16] M. Sundararaman, P. Mukhopadhyay, S. Banerjee, Some aspects of the precipitation of metastable intermetallic phases in INCONEL 718, Metall. Trans. A 23 (7) (1992) 2015–2028.
[17] S. Azadian, L.Y. Wei, R. Warren, Delta phase precipitation in inconel 718, Mater. Charact. 53 (2004) 7–16.
[18] K.-M. Chang, H.-J. Lai, J.-Y. Hwang, Existence of Laves phase in Nb-hardened superalloys, Miner. Met. Mater. Soc. (1994) 683–694, vol. Superalloy.
[19] L. Zhu, Z. Xu, Y. Gu, Effect of laser power on the microstructure and mechanical properties of heat treated Inconel 718 superalloy by laser solid forming, J. Alloys Compd. 746 (2018) 159–167.
[20] H. Xiao, S. Li, X. Han, J. Mazumder, L. Song, Laves phase control of Inconel 718 alloy using quasi-continuous-wave laser additive manufacturing, Mater. Des. 122 (2017) 330–339.
[21] J. Ding, et al., Thermo-mechanical analysis of wire and arc additive layer manufacturing process on large multi-layer parts, Comput. Mater. Sci. 50 (12) (2011) 3315–3322.
[22] P.A. Colegrove, et al., Microstructure and residual stress improvement in wire and arc additively manufactured parts through high-pressure rolling, J. Mater. Process. Technol. 213 (2013) 1782–1791.
[23] F. Martina, et al., "Residual stress of as-deposited and rolled wire+arc additive manufacturing Ti–6Al–4V components, Mater. Sci. Technol. 32 (14) (2016) 1439–1448.
[24] J.R. Hönnige, S. Williams, M.J. Roy, P. Colegrove, S. Ganguly, Residual stress characterization and control in the additive manufacture of large scale metal structures, in: 10th International Conference On Residual Stresses, 2016.
[25] J.R. Hönnige, et al., Residual stress and texture control in Ti-6Al-4V wire+arc additively manufactured intersections by stress relief and rolling, Mater. Des. 150 (2018) 193–205.
[26] J.R. Hönnige, P.A. Colegrove, S. Ganguly, E. Eimer, S. Kabra, S.W. Williams, Control of residual stress and distortion in aluminium wire + arc additive manufacture with rolling, Addit. Manuf. 22 (2018) 775–783.
[27] J.R. Hönnige, P.A. Colegrove, S.W. Williams, Analytical process model for wire + arc additive manufacturing, Mater. Res. Proc. 6 (2018) 277–282.
[28] M.J. Bermingham, L. Nicastro, D. Kent, Y. Chen, M.S. Dargusch, Optimising the mechanical properties of Ti-6Al-4V components produced by wire þ arc additive manufacturing with post-process heat treatments, J. Alloys Compd. 753 (2018) 247–255.
[29] X. Zhang, F. Martina, J. Ding, X. Wang, S. Williams, "Fracture toughness and fatigue crack growth rate properties in wire + arc additive manufactured Ti-6Al-4V, Fatigue Fract. Eng. Mater. Struct. (2016) 1–14.
[30] J. Zhang, X. Wang, S. Paddea, X. Zhang, Fatigue crack propagation behaviour in wire + arc additive manufactured Ti-6Al-4V: effects of microstructure and residual stress, Mater. Des. Des. 90 (2016) 551–561.
[31] E.R. Denlinger, J.C. Heigel, P. Michaleris, T.A. Palmer, Effect of inter-layer dwell time on distortion and ResidualStress in additive manufacturing of titanium and nickel alloys, J. Mater. Process. Technol. 215 (2015) 123–131.
[32] F. Bayerlein, F. Bodensteiner, C. Zeller, M. Hofmann, M.F. Zaeh, Transient development of residual stresses in laser beam melting - a neutron diffraction study, Addit. Manuf. 24 (2018) 587–594.
[33] T. Thiede, et al., Residual stress in selective laser melted inconel 718: influence of the removal from base plate and deposition hatch length, Mater. Perform. Charact. 7 (4) (2018).

[34] K. An, L. Yuan, L. Dial, I. Spinelli, A.D. Stoica, Y. Gao, "Neutron residual stress measurement and numerical modeling in a curved thin-walled structure by laser powder bed fusion additive manufacturing ☆, Mater. Des. 135 (2017) 122–132.
[35] N. Nadammal, et al., Effect of hatch length on the development of microstructure , texture and residual stresses in selective laser melted superalloy Inconel 718, Mater. Des. 134 (2017) 139–150.
[36] О.Ю. СМетанников, et al., Modeling of the product termomechanical behavior during 3D deposition of wire materials in ansys, PNRPU Mech. Bull. (4) (2017) 154–172.
[37] X. Xu, S. Ganguly, J. Ding, C.E. Seow, S. Williams, "Enhancing mechanical properties of wire + arc additively manufactured INCONEL 718 superalloy through in-process thermomechanical processing, Mater. Des. 160 (2018) 1042–1051.
[38] B. Baufeld, Mechanical properties of INCONEL 718 parts manufactured by shaped metal deposition (SMD), J. Mater. Eng. Perform. 21 (7) (2012) 1416–1421.
[39] G.P. Dinda, A.K. Dasgupta, J. Mazumder, Texture control during laser deposition of nickel-based superalloy, Scr. Mater. 67 (5) (2012) 503–506.
[40] D. Ma, A.D. Stoica, Z. Wang, A.M. Beese, Crystallographic texture in an additively manufactured nickel-base superalloy, Mater. Sci. Eng. A 684 (2017) 47–53.
[41] Z. Wang, A.D. Stoica, D. Ma, A.M. Beese, Diffraction and single-crystal elastic constants of Inconel 625 at room and elevated temperatures determined by neutron diffraction, Mater. Sci. Eng. A 674 (2016) 406–412.
[42] M.A. Rist, S. Tin, B.A. Roder, J.A. James, M.R. Daymond, Residual stresses in a quenched superalloy turbine disc: measurements and modeling, Metall. Mater. Trans. A 37 (2) (2006) 459–467.
[43] P.E. Aba-Perea, T. Pirling, M. Preuss, In-situ residual stress analysis during annealing treatments using neutron diffraction in combination with a novel furnace design, Mater. Des. 110 (2016) 925–931.
[44] H. Monajati, F. Zarandi, M. Jahazi, S. Yue, "Strain induced γ′ precipitation in nickel base superalloy Udimet 720 using a stress relaxation based technique, Scr. Mater. 52 (8) (2005) 771–776.
[45] T. Pirling, G. Bruno, P.J. Withers, SALSA-A new instrument for strain imaging in engineering materials and components, Mater. Sci. Eng. A 437 (2006) 139–144.
[46] Z. Zhou, et al., Experimental and finite element simulation study of thermal relaxation of residual stresses in laser shock peened IN718 SPF superalloy, Exp. Mech. 54 (9) (2014) 1597–1611.
[47] H.E. Coules, Contemporary approaches to reducing weld-induced residual stress, Mater. Sci. Technol. 29 (1) (2012).
[48] W.T. Han, F.R. Wan, G. Li, C.L. Dong, J.H. Tong, Effect of trailing heat sink on residual stresses and welding distortion in friction stir welding Al sheets 16 (5) (2011) 453–458.
[49] L. Parry, I.A. Ashcroft, R.D. Wildman, Understanding the effect of laser scan strategy on residual stress in selective laser melting through thermo-mechanical simulation, Addit. Manuf. 12 (2016) 1–15.
[50] G. Vastola, G. Zhang, Q.X. Pei, Y.-W. Zhang, Controlling of residual stress in additive manufacturing of Ti6Al4V by finite element modeling, Addit. Manuf. (2016).
[51] E.R. Denlinger, P. Michaleris, Effect of stress relaxation on distortion in additive manufacturing process modeling, Addit. Manuf. 12 (2016) 51–59.
[52] V.I. Kurkin, S.A. Anufriev, "Preventing distortion of welded thin-walled members of AMg6 and 1201 aluminum alloys by rolling the weld with a roller behind the welding arc, Sverochnoe Proizv. 31 (10) (1984) 52–55.
[53] J. Altenkirch, A. Steuwer, P.J. Withers, S.W. Williams, M. Poad, S.W. Wen, Residual stress engineering in friction stir welds by roller tensioning, Sci. Technol. Weld. Join. 14 (2) (2009) 185–192.
[54] H.E. Coules, P. Colegrove, L.D. Cozzolino, S.W. Wen, S. Ganguly, T. Pirling, Effect of high pressure rolling on weld-induced residual stresses, Sci. Technol. Weld. Join. 17 (5) (2012) 394–401.
[55] J. Gu, J. Ding, S.W. Williams, H. Gu, P. Ma, Y. Zhai, The effect of inter-layer cold working and post-deposition heat treatment on porosity in additively manufactured aluminum alloys, J. Mater. Process. Technol. 230 (2016) 26–34.
[56] F. Martina, P.A. Colegrove, S.W. Williams, J. Meyer, Microstructure of interpass rolled wire + arc additive manufacturing Ti-6Al-4V components, Metall. Mater. Trans. A Phys. Metall. Mater. Sci. 46 (12) (2015) 6103–6118.
[57] P.A. Colegrove, J. Donoghue, F. Martina, J. Gu, P. Prangnell, J. Hönnige, Application of bulk deformation methods for microstructural and material property improvement and residual stress and distortion control in additively manufactured components, Scr. Mater. 2 (2016).
[58] J. Gu, J. Ding, S.W. Williams, H. Gu, P. Ma, Y. Zhai, "The strengthening effect of inter-layer cold working and post-deposition heat treatment on the additively manufactured Al–6.3Cu alloy, Mater. Sci. Eng. A 651 (2016) 18–26.
[59] S. Tammas-Williams, P.J. Withers, I. Todd, P.B. Prangnell, Porosity regrowth during heat treatment of hot isostatically pressed additively manufactured titanium components, Scr. Mater. 122 (2016) 72–76.
[60] G. Appa Rao, M. Srinivas, D.S. Sarma, Effect of thermomechanical working on the microstructure and mechanical properties of hot isostatically pressed superalloy Inconel 718, Mater. Sci. Eng. A 383 (2004) 201–212.
[61] H.J. Stone, T.M. Holden, R.C. Reed, Determination of the plane specific elastic constants of Waspaloy using neutron diffraction, Scr. Mater. 40 (3) (1999) 353–358.
[62] T. Mishurova, et al., The influence of the support structure on residual stress and distortion in SLM inconel 718 parts, Metall. Mater. Trans. A 49A (7) (2018) 3038–3046.
[63] J. Repper, M. Hofmann, C. Krempaszky, W. Petry, E. Werner, Influence of microstructural parameters on macroscopic residual stress analysis of complex materials by neutron diffraction methods, Mater. Sci. Forum 571–572 (2008) 39–44.
[64] P.J. Withers, M. Preuss, A. Steuwer, J.W.L. Pang, Methods for obtaining the strain-free lattice parameter when using diffraction to determine residual stress, J. Appl. Crystallogr. 40 (5) (2007) 891–904.
[65] K.N. Amato, et al., Microstructures and mechanical behavior of Inconel 718 fabricated by selective laser melting, Acta Mater. 60 (5) (2012) 2229–2239.
[66] M. Sundararaman, P. Mukhopadhyay, "Overlapping of γ'' recipitate variants in Inconel 718, Mater. Charact. 31 (4) (1993) 191–196.
[67] S. Luo, W. He, K. Chen, X. Nie, L. Zhou, Y. Li, Regain the fatigue strength of laser additive manufactured Ti alloy via laser shock peening, J. Alloys Compd. 750 (2018) 626–635.
[68] C. Radhakrishna, K. Prasad Rao, The formation and control of Laves phase in superalloy 718 welds, J. Mater. Sci. 32 (8) (1997) 1977–1984.
[69] J. Sule, S. Ganguly, H. Coules, T. Pirling, Application of local mechanical tensioning and laser processing to refine microstructure and modify residual stress state of a multi-pass 304L austenitic steels welds, J. Manuf. Process. 18 (2015) 141–150.
[70] J. Donoghue, A.A. Antonysamy, F. Martina, P.A. Colegrove, S.W. Williams, P. B. Prangnell, The effectiveness of combining rolling deformation with Wire-Arc Additive Manufacture on β-grain refinement and texture modification in Ti-6Al-4V, Mater. Charact. 114 (2016) 103–114.
[71] J.M. Zhang, Z.Y. Gao, J.Y. Zhuang, Z.Y. Zhong, Grain growth model of IN718 during holding period after hot deformation, J. Mater. Process. Technol. 101 (2000) 25–30.
[72] H.Y. Zhang, S.H. Zhang, M. Cheng, Z. Zhao, Microstructure evolution of IN718 alloy during the delta process, in *Procedia Engineering* 207 (2017) 1099–1104.
[73] J.J. Ruan, N. Ueshima, K. Oikawa, Phase transformations and grain growth behaviors in superalloy 718, J. Alloys Compd. 737 (2018) 83–91.
[74] J.I. Goldstein, D.E. Newbury, J.R. Michael, N.W.M. Ritchie, J.H.J. Scott, D.C. Joy, Scanning Electron Microscopy and X-Ray Microanalysis, vol. 6, 2017, 4.
[75] A. Mitchell, A.J. Schmalz, C. Schvezov, S.L. Cockroft, The precipitation of primary carbides in alloy 718, in: *Superalloys* 718, 625, 706 and Various Derivatives, 1994, pp. 65–78, 1994.
[76] G. Korovsky, M. Cieslak, T. Headley, A. Romig, W. Hammetter, Inconel 718: a solidification diagram, Metall. Trans. A 20A (1989) 2149–2158. October.
[77] J. Ding, P. Colegrove, J. Mehnen, S. Williams, F. Wang, P.S. Almeida, A computationally efficient finite element model of wire and arc additive manufacture, Int. J. Adv. Manuf. Technol. 70 (2014) 227–236.
[78] M. Tomlin, J. Meyer, Topology optimization of an additive layer manufactured (ALM) aerospace part, in: The 7th Altair CAE Technology Conference, 2011, pp. 1–9.